


Boundless Metamaterial Experimentation: Physical Realization of a Unidirectional Virtual Periodic Boundary Condition

Henrik R. Thomsen¹,* Bao Zhao¹, and Andrea Colombi¹

Department of Civil, Environmental and Geomatic Engineering, ETH Zurich, Stefano-Franscini-Platz 5, Zurich 8093, Switzerland

 (Received 18 January 2023; revised 30 March 2023; accepted 21 April 2023; published 6 June 2023)

We experimentally implement a one-directional virtual geometric periodicity in an elastic metamaterial. First, unwanted boundary reflections at the domain ends are cancelled through the iterative injection of the polarity-reversed reflected wave field. The resulting boundless experimental state allows for a much better analysis of the influence of metamaterials on the propagating wave field. Subsequently, the propagating wave field exiting on one end of the structure is reintroduced at the opposite end, creating a virtual geometric periodicity in one propagation direction. We find that the experimentally observed band gap converges to the analytical solution through the introduction of the virtual periodicity. The established work flow introduces an approach to the experimental investigation and validation of metamaterial prototypes in the presence of strongly dispersive wave propagation and internal scattering. The fully data-driven *ad hoc* treatment of boundary conditions in metamaterial experimentation with arbitrary mechanical properties enables reflection suppression, virtual periodicity, and the introduction of more general fictitious boundaries.

DOI: [10.1103/PhysRevApplied.19.064019](https://doi.org/10.1103/PhysRevApplied.19.064019)

I. INTRODUCTION

Engineered metamaterials have long since proven their capabilities to exhibit extraordinary material properties [1–3], as well as to manipulate and attenuate wave propagation [4,5] using band gaps. Such prohibited frequency ranges can be architected into materials via either Bragg-scattering phononic crystals [6] or locally resonant metamaterials [7]. The latter enable subwavelength band gaps [8] and have recently been leveraged for broadband energy harvesting [9–12]. Numerical simulations drive the development of metamaterials, the ever-increasing available computational power making it feasible to rapidly model different designs. Nevertheless, experimental investigation and validation of prototype structures remains essential. Whereas in numerical studies, effects such as low-absorbing boundary layers or local damping [13,14] can be introduced to simulate free-space wave propagation, laboratory experiments are often plagued by modal responses of the system caused by, e.g., free or clamped boundaries. Additionally, wave propagation within the structure is difficult to interpret due to boundary reflections. Thus, it is often challenging to accurately distinguish phenomena caused by the metamaterial under study from those of the whole system. Conventional experimental solutions to these pitfalls are passive boundary reflection damping, such as acoustic black holes [15–18], or graded impedance

interfaces [19]. However, these practices result in modifications of the host structure, which in turn can lead to deviations from the desired system response.

A promising alternative is elastic “immersive wave experimentation” (IWE) [20], used to actively remove the unwanted boundary reflections at the domain ends of a solid target, such as an elastic metamaterial wave guide. IWE is an experimental methodology aimed at overcoming laboratory- and sample-size-related limitations that affect conventional wave-propagation experimentation. This is achieved by linking wave propagation between a physical experimental domain and a desired virtual domain through modification of the physical boundary conditions encountered in the laboratory [21]. The method can be used in a wide range of applications, such as cloaking and holography [22], as well as virtual extension [20] and modification [23] of the finite physical domain encountered in the laboratory. A proposal has also been made to utilize acoustic IWE in the implementation of arbitrary experimental periodic boundary conditions by cancelling reflections on one end of a structure and reintroducing the propagating wave field on the opposite side [24]. If successfully employed, this would allow us to study the effect of, e.g., phononic crystals or locally resonant metamaterials without the need to physically realize large structures in the laboratory but, instead, only a few unit cells. Integral to IWE is the correct identification of the first-order incident event at the domain boundaries, i.e., wave energy that has not interacted with said boundaries before. This event is then used

*thomsenh@ethz.ch

to construct a secondary force signature that when applied at, e.g., the free ends of an aluminum beam, leads to the cancellation of the reflected energy, creating a transparent boundary that can then be fully controlled and linked to an arbitrary virtual domain, if desired.

Our work demonstrates the first use case of elastic IWE and significantly expands on the method in two key aspects: (1) the frequency range of interest is <1 kHz, rather than tens of kilohertz; and (2) we focus on flexural (Lamb) waves propagating along a graded beam characterized by strong dispersion and internal scattering. Such wave propagation is often encountered in metamaterials research and isolation of the first-order reflected wave field cannot be easily achieved due to the strong dispersion and scattering. In this context, the cancellation of reflections originating at the ends of the structure allows us to clearly analyze the modulation of the wave when passing through, e.g., the graded area of a prototype metamaterial.

In the following, we first introduce our proposed work flow to implement elastic “immersive boundary control” in the experimental domain. We schematically showcase how to effectively cancel boundary reflections in three cases often encountered in physical experiments, with a focus on metamaterials: (1) the base-case single-sided IWE, where a clear identification of the incident or reflected wave field at the structures boundaries is possible; (2) iterative single-sided IWE, where the clear identification of the incident and/or reflected wave field is not possible due to, e.g., the presence of strong dispersion; and (3) double-sided IWE, with internal scattering caused by strong impedance contrasts due to, e.g., the design of the metamaterial, requiring, again, the utilization of an iterative procedure. The proposed work flow is then used to successfully remove unwanted boundary reflections from a metamaterial designed for energy-harvesting purposes [12] and to create a one-directional virtual geometric periodicity in the elastic experiment.

II. ITERATIVE PROCEDURE TO IMPLEMENT IMMERSIVE BOUNDARY CONDITIONS

Elastic IWE states that applying the incident traction as an auxiliary force on the free surface of an experimental domain, such as the face of a rock or the ends of an aluminum beam, results in a cancellation of the wave field reflected at said boundary, accounting for any mode conversions. Thomsen *et al.* [20] have shown that this effect can be implemented experimentally by applying the polarity-flipped first-order reflected wave field at the free-surface ends of the physical domain under investigation, allowing for the cancellation of both reflected longitudinal and flexural wave modes. A first-order reflection describes an event that has not interacted with the domain ends before. Different to acoustic IWE, as presented by, e.g., Becker *et al.* [23] and Börsing *et al.* [22], elastic IWE is

nearly impossible to implement in real time because of the high wave-propagation velocities. This leads to an unfeasible small lag time to predict the incident wave field before it reaches the boundary. Therefore, the desired immersive experimental state is built up iteratively. Key is the correct identification of the incident and reflected wave fields. Possible methods to achieve this are, e.g., wave-field injection [25], redatuming [26], and f - k domain filtering [27]. The latter is used in our proposed work flow.

A. Case 1: Single-sided IBC and clear incident or reflected wave identification

The most straightforward procedure to implement immersive boundary conditions (IBCs) is through injection of the polarity-reversed first-order reflected wave measured at the ends of the experimental domain. Figure 1(a) schematically shows a one-dimensional example of a longitudinal wave propagating back and forth between two free ends over time. The wave field is induced on the left side by the source (SRC). Identification and isolation of the first event reflected at the right end (indicated by the “1”) results in the design of the IBC: the polarity-reversed version of said event. When injected on the right, as indicated by IBC A in Fig. 1(b), the first reflection that occurs is effectively cancelled and any higher-order reflections cease to exist. This procedure is used if the first-order reflected event can be clearly identified.

B. Case 2: Single-sided IBC and iterative procedure

Unfortunately, a clear identification of just the required first-order reflected event is not always possible, especially when dealing with strongly dispersive wave propagation or internal reflection. In such cases, the desired boundary

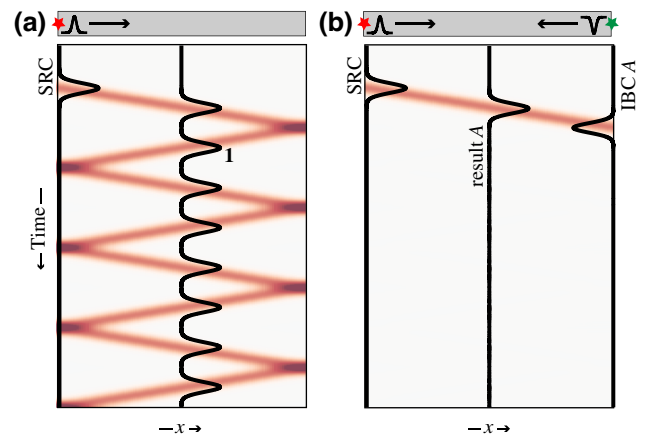


FIG. 1. A conceptual representation of time-distance plots for case 1: single-sided and clear incident or reflected wave identification. (a) The initial experimental state. (b) The result when cancelling the reflected events by injecting the polarity-reversed first-order reflected event at the right end. The applied IBC is indicated by a black trace on the right end of the plot.

control can still be achieved through the use of the iterative procedure proposed herein.

Starting with the initial experimental state displayed in Fig. 2(a), rather than injecting just the polarity-reversed version of the first reflected event, the *full* reflected wave field, labeled “1” to “4,” i.e., the wave field propagating to the left, is injected as indicated by IBC *A* on the right end of Fig. 2(b). As a result, the first-order reflected event is removed, as can be seen in the same figure. This results in all higher-order events ceasing to exist, as in case 1. However, by applying the polarity-reversed *full* reflected wave field, new energy is actively injected into the system. Thus, the second-order event can now be found propagating at opposite polarity to the initial experimental state. Additionally, the wave field is amplified for every higher interaction with the right end due to the constructive interference of the propagating wave field with the continued injection of higher-order reflected events as part of the initial IBC *A*. These unwanted events are eventually removed by repeating the experiment and using the consecutive

experimental states to iteratively modify the IBC. The final IBC only applies the first-order reflected wave field without introducing unwanted wave-field propagation.

This is achieved by isolating the new wave field reflected at the right end as indicated by “2” to “4” in Fig. 2(b), reversing it in polarity and adding it to the previously applied IBC *A*. The resulting IBC *B* is shown in Fig. 2(c). Here, the second-order event is removed from the trace of IBC *B*. Thus, one higher-order event less is reintroduced to the experimental state during the application of IBC *B*. Figure 2(d) then shows how IBC *B*, when applied, removes both the first- and second-order reflections, yet still introduces the third- and amplified higher-order events. Finally, by repeating the process an additional 2 times, IBC *D* in Fig. 2(f) matches IBC *A* from Fig. 1(b) in the time range shown.

In summary, the iterative procedure removes the unwanted higher-order reflected events step by step. The IBC, initially containing the *full* reflected wave field, converges to the first-order reflected wave field.

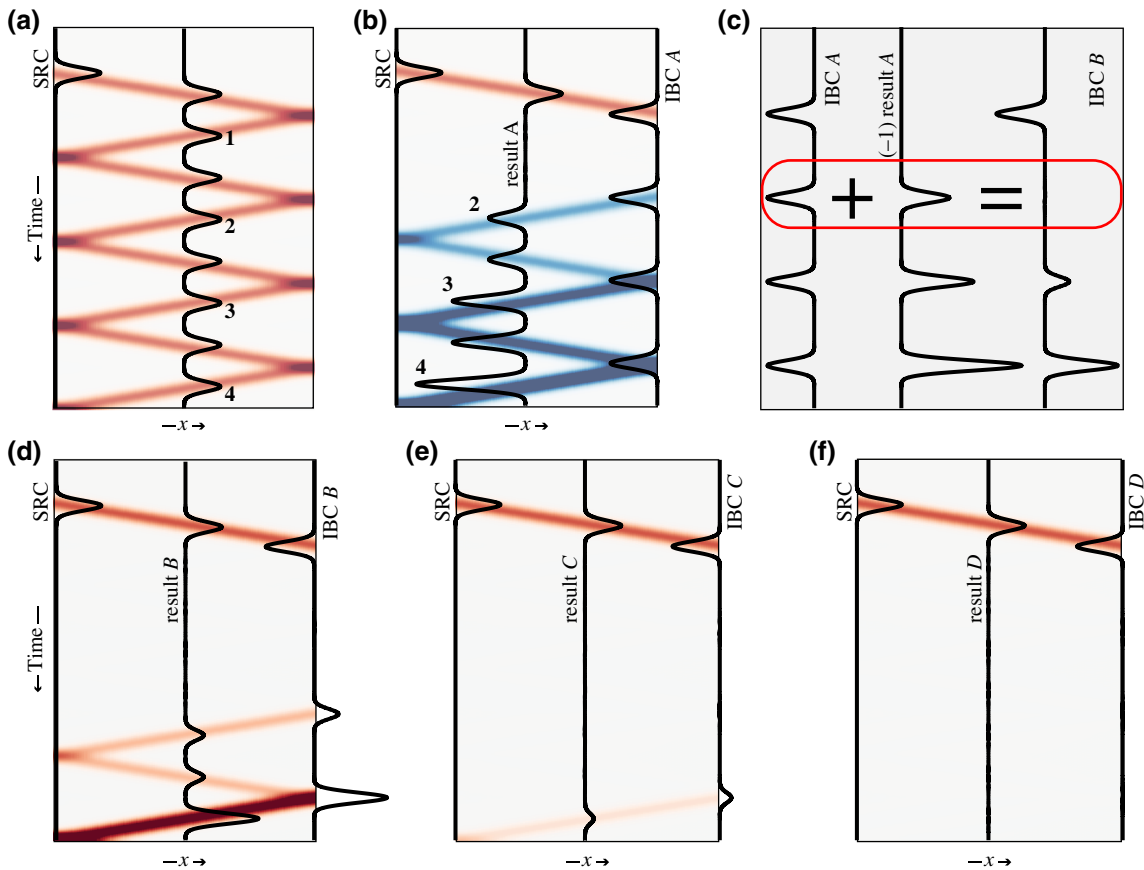


FIG. 2. A conceptual representation of time-distance plots for case 2: the single-sided and iterative procedure to remove boundary reflections. (a) The initial experimental state. (b),(d)–(f) The evolution of the IBC applied to the right end, as indicated by the black trace, as well as the resulting wave propagation. (c) How the IBC is iteratively modified by adding the currently applied IBC and the resulting polarity-reversed reflected wave field.

C. Case 3: Double-sided IBC with internal scattering present

The iterative method to construct the IBC described above can also be used when reflections occur not only at the ends but also within the structure, as schematically displayed in Fig. 3(a). In this example, an internal impedance contrast, indicated by the gray-shaded area, causes internal scattering. Such cases are commonly encountered when investigating metamaterials where, e.g., resonators introduce frequency-dependent impedance contrasts in the medium. The internal impedance contrast results in two types of undesired boundary reflections: those transmitted through the structure and reflected at the ends and those radiated internally and then interacting with the end boundaries.

Therefore, the construction of the IBC requires a double-sided iterative procedure to construct the desired boundless experimental state where only primary wave propagation remains. In Fig. 3(a), we can observe first-order reflections on both the left and right ends, as indicated by $1L$ and $1R$, respectively, as well as higher-order events ($2L$ – $4L$, $2R$, and $1L1R$ – $2L1R$). In a first step, the complete wave field reflected at the left end is reversed in polarity and injected together with the source wave field. The

result, displayed in Fig. 3(b), shows how both first-order reflections ($1L$) are removed on the left side. The higher-order events are again amplified as previously described in case 2. Additionally, the reflection on the right side (event $1L1R$), originating from event $1L$, is also removed in Fig. 3(b). Next, the full reflected wave field acquired on the right side of the new experimental state, displayed in Fig. 3(b), is reversed in polarity and injected at the right end. As a result, the reflection of event $1R$ is cancelled and event $2R$ is flipped in polarity, as can be observed in Fig. 3(c). Next, the IBC on the left end is updated with the new experimental state, resulting in the removal of event $2L$, as shown in Fig. 3(d). This iterative process of applying and then constructing the IBC wave field on opposite sides is repeated several more times [Figs. 3(e)–3(g)], until the left and right IBC wave fields, displayed as black time traces at the ends of Fig. 3(g), only contain the first-order reflected events when compared to the initial IBC shown in Fig. 3(c). The final boundless experimental state when applying the double-sided IBC is shown in Fig. 3(g). All undesired reflections at the boundaries are removed and only the propagation of the primary scattered wave field remains.

Note that the iterative procedure described cancels the unwanted boundary reflections up to a cutoff time defined

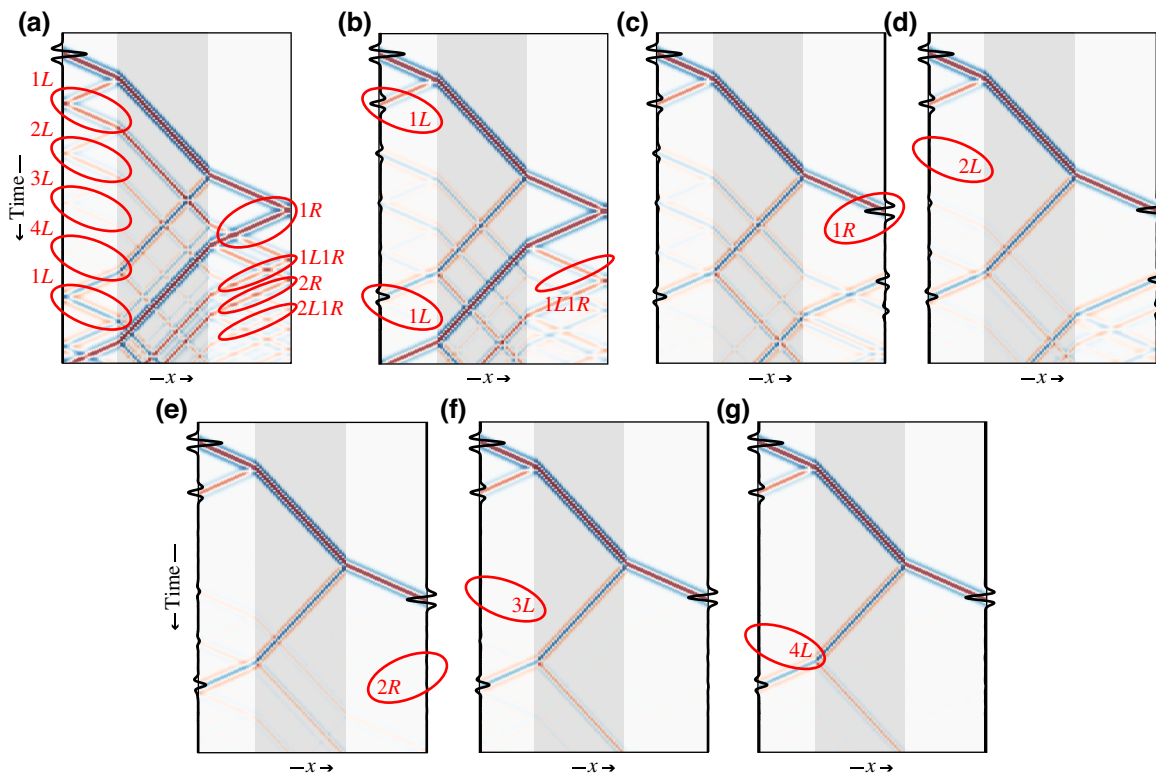


FIG. 3. A conceptual illustration of time-distance plots for case 3: double-sided IBC with internal scattering due to an impedance contrast indicated in gray. (a) The initial experimental state. (b)–(f) The evolution of the IBC applied to the right and left ends, as well as the resulting wave propagation. (g) The final experimental state after the left and right IBCs converge to only applying the polarity-reversed first-order events and the resulting primary wave-field propagation.

by the iteration step, i.e., the order of reflected events currently removed. Wave propagation after this time is amplified due to the constructive interference of the injected IBC wave field and propagating waves. Thus, increased damping in the system under investigation can be advantageous, as it would reduce the required iteration steps to achieve the desired experimental state.

III. EXPERIMENTALLY IMPLEMENTED VIRTUAL PERIODIC BOUNDARY

We now experimentally demonstrate the implementation of a virtual periodic boundary along one propagation direction using IWE to aid in the investigation of a graded metamaterial. The prototype structure under investigation is shown in Fig. 4(a). It is made up of a 2-mm-thick 1-m-long host beam endowed with “wings” of increasing length arranged in the central region spanning 30 cm (from 0.3–0.6 m). The wings form a graded metasurface, which acts as a spatial-frequency filter on the propagating wave while simultaneously slowing down the group velocity of the traveling wave. This metamaterial has been designed by Zhao *et al.* [12] for broadband and high-capability energy harvesting at low-frequency ambient noise vibrations. First, we construct and apply an IBC on the right and left ends of the host beam to cancel the reflections and create transparent boundaries. Following this, the wave field incident on the right end is reintroduced to the structure on the left end to create a virtual geometric periodicity for waves propagating to the right in the metamaterial.

A. The metamaterial under investigation

A flexural plane wave is induced on the left end by a piezoelectric actuator (P. 153.05 [28]). The same type of actuator is also attached to the beam on the opposite end. Both actuators act as IBC sources to control their respective boundaries. Additionally, two 44.3-g counterweights are attached to the respective ends of the beam. Together with the actuator, they create a symmetric boundary condition. Testing shows that when only the piezoelectric actuator is attached to the ends of the beam, undesired mode conversions occur during wave reflection. Adding the actuators modifies the boundary conditions at the ends of the beam. However, contrary to conventional reflection-mitigation methods, we retain full control of the boundary response through the application of the IBC. The out-of-plane velocity is measured in the time domain along the beam using a robotized 3D laser Doppler vibrometer [29] as illustrated in Fig. 4(a). The data are recorded for 100 ms with a sampling frequency of $f_s = 100$ kHz and averaged 5 times at each of the 101 measurement points, spaced 1 cm apart along the beam. A 500-Hz (central frequency) Ricker wavelet, with a peak amplitude of 100 V, is driven to the out-of-plane component of the actuator placed on the left

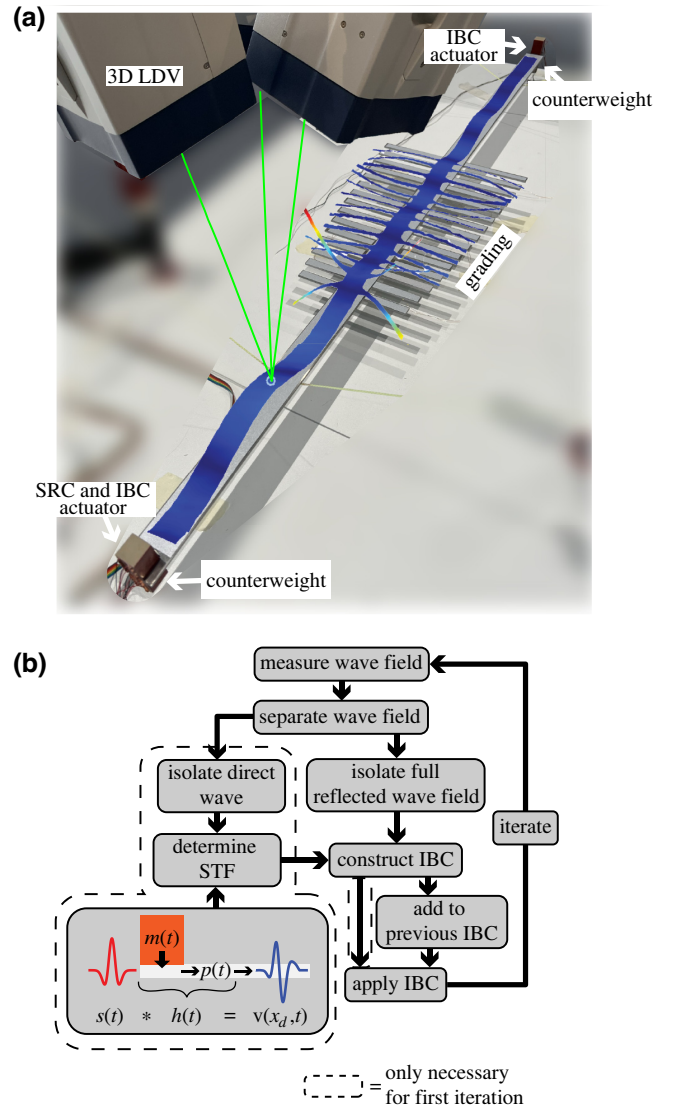


FIG. 4. (a) The experimental setup. A piezoelectric actuator and counterweight are attached to both ends of the beam. The three-dimensional (3D) laser Doppler vibrometer is used to measure the out-of-plane wave-field propagation. Overlain is a snapshot of the out-of-plane velocity recordings along the full structure at 12.88 ms. (b) The work flow to iteratively construct and apply the IBC. The dashed lines indicate steps only required for the first iteration.

end of the beam. Figure 5(a) depicts a time-distance representation of the resulting out-of-plane flexural wave (A_0 Lamb mode) traveling along the beam for the initial 25 ms. The strongly dispersive nature of the propagating flexural wave, as well as the strong internal scattering occurring due to the large impedance contrast imposed by the graded area, are apparent.

The effect of a metamaterial on the propagating wave is commonly investigated through analyzing the normalized spatial-frequency distribution along the structure, as depicted in Fig. 5(c). The length of the wings attached to

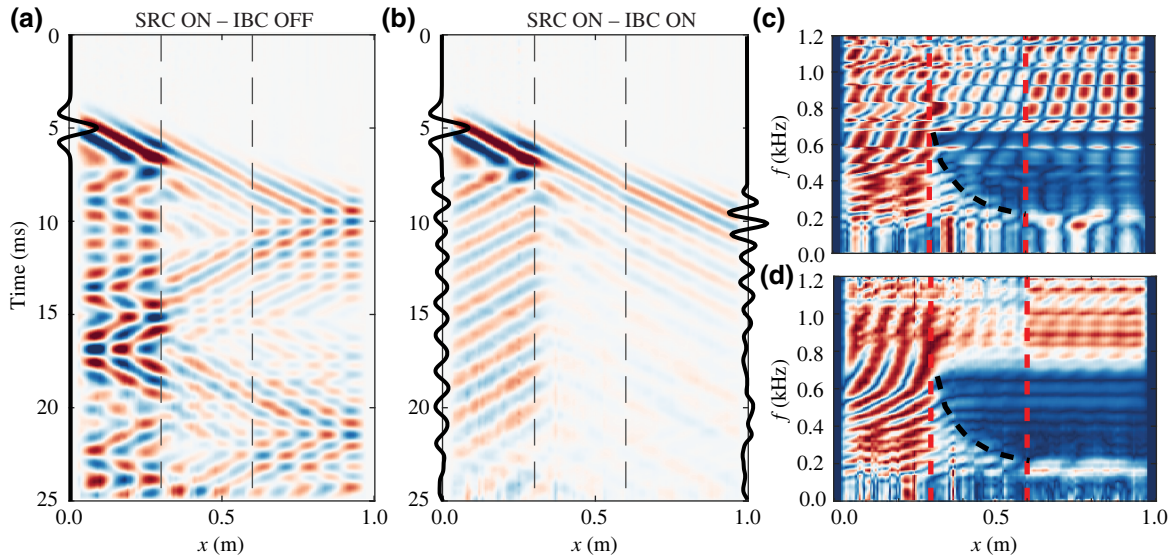


FIG. 5. A time-distance representation of the out-of-plane velocity measured along the beam. The vertical dashed lines indicate the graded area. (a) Source ON (illustrated by the black line on the left) and IBC OFF. (b) Source ON and IBC ON (illustrated by the black lines on the left and right). (c),(d) The spatial-frequency distribution, normalized for each frequency, along the structure with the IBC OFF and ON, respectively. The black dashed lines track the band gap. Animations of the wave propagation along the structure, scanned by the 3D LDV, for both (a) and (b), can be found in Movies 00 and 01 in the Supplemental Material [30].

the host beam evolves from short to long. Consequently, higher frequencies are filtered out earlier along the graded area than the lower frequencies. Thus, the frequency content of the wave field incident on the graded area is modified through interaction with it. A phenomenon referred to as rainbow trapping [4,31,32]. Overall, the metamaterial induces a band gap from 200 to 680 Hz. A peak in the spatial-frequency content at 585 Hz, protruding into the band gap, is noticeable. As we show later, this mode shape is a result of the boundary reflections occurring at the ends of the host beam.

A clear understanding of the frequencies at which the individual wings comprising the graded metastructure resonate at is also crucial during the experimental investigation of the prototype. Such insights are important when optimizing the grading profile and the resulting band gap. As an example, the red (dark) lines in Figs. 6(a) and 6(b) depict both the out-of-plane velocity and the frequency spectrum measured at the tip of wing 13. Strong peaks in the frequency response can be observed at both 220 and 805 Hz, showing how the reflections at the ends of the structure can make a clear identification of the resonance frequency difficult.

B. Step 1: Reflection removal

We use case 3 described above to remove the undesired boundary reflections, i.e., the IBC is constructed iteratively on both ends. First, the full wave field reflected at the left and right end has to be determined and applied

as the IBC. Hence, the out-of-plane component ($v(x, t)$) measured along the beam is separated into its rightward- ($r(x, t)$) and leftward- ($l(x, t)$) propagating components. In the f - k -domain representation of the data, the rightward- and leftward propagating wave fields map into opposite

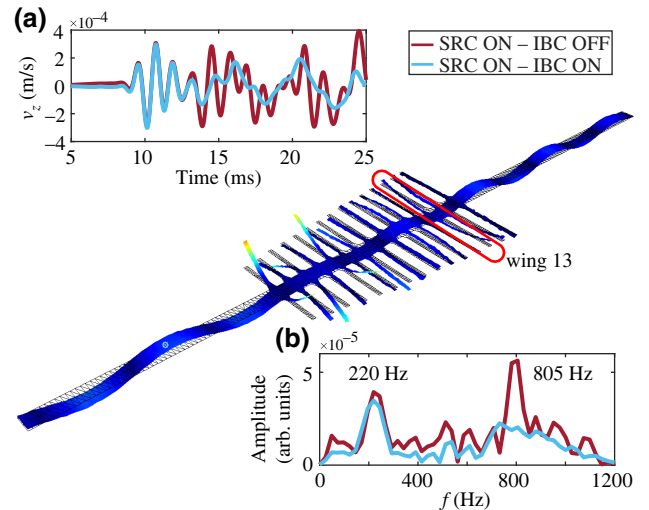


FIG. 6. A snapshot of the wave propagation recorded via the 3D LDV at 19.50 ms: the (a) time series and (b) the frequency spectra of the out-of-plane velocity recorded at the tip of wing 13. The red (dark) lines indicate the experimental state with boundary reflections present (SRC ON–IBC OFF) and the blue (light) lines those with cancelled boundary reflections (SRC ON–IBC ON).

quadrants and can be separated using a masking filter [27]. However, before applying the full reflected wave field at the respective end of the beam and iteratively realizing the IBC, an additional step is required when working with laboratory data. As the IBC is applied via the two actuators at the ends, we must first determine which voltage signal $s(t)$ to apply to the actuators to induce the desired wave-field propagation $v(x_d, t)$ at any point x_d along the beam, namely, the IBC signature [20] [see the schematic at the bottom of the work flow in Fig. 4(b)]. To this end, a source transfer function (STF) $h_{\text{LS-RS}}^{-1}(t)$ for both the left (LS) and the right (RS) actuators must be found that accounts for both the mechanical response of the actuator ($m(t)$) and propagation ($p(t)$) along the beam to the measurement point at a distance x_d to the source. The left and right ends of the beam are excited via the actuators and the STF determined using a measurement at a distance of $x_d = 0.1$ m from the respective ends of the beam. We then isolate the propagating direct wave ($v_d(x_{\text{LS,RS}}, t)$), which must be clearly identifiable after wave-field separation, measuring at $x_{\text{LS}} = 0.1$ m and $x_{\text{RS}} = 0.9$ m, respectively. The STF $h_{\text{LS-RS}}^{-1}(t)$ is eventually calculated by optimally matching the isolated direct wave to the original source signal ($s(t)$) applied to the actuator in a least-squares sense. A reliable estimation of the STF allows for an implementation of the IBC without any further assumptions about the medium required, such as, e.g., propagation speeds or the f - k relation. Thus, the method is fully data driven. Finally, the polarity-reversed total reflected rightward- ($-r(x, t)_{\text{refl}}$) and leftward- ($-l(x, t)_{\text{refl}}$) propagating wave fields are convolved with the STF $h_{\text{LS-RS}}^{-1}(t)$ and injected at the ends of the beam in the iterative and alternating manner described by case 3, resulting in the desired experimental state with the boundary reflections removed as shown in Fig. 5(b). This work flow is summarized by the flow chart depicted in Fig. 4(b). The final IBC signature shown by the black traces on the left and right ends of Fig. 5(b) removes the first-order reflection, as well as all higher-order reflected events at the domain ends up to a time of 25 ms. The corresponding normalized spatial-frequency distribution along the structure is depicted in Fig. 5(d). We observe that the peak in the spatial-frequency content at 585 Hz present in Fig. 5(c) is absent due to the removal of the boundary reflections. Overall, the induced band gap between 200 and 680 Hz is also more clearly discernible. Finally, an analysis of the frequency response measured at the tip of wing 13 also shows a mitigation of the strong peak at 805 Hz [see Fig. 6(b)], making it clear that the wing resonates at 220 Hz.

C. Step 2: Introducing an experimental virtual periodicity

Once the reflections are removed, we experimentally introduce a virtual periodic boundary condition in

one propagation direction. To this end, the rightward-propagating wave field, impinging on the right end of the beam after passing through the graded area, is isolated and reintroduced on the left end of the beam. Since the wave field cannot be measured directly at the beam ends due to the presence of the actuators, it is measured at $x_1 = 0.85$ m and forward extrapolated to the right end of the beam at $x_2 = 1.0$ m before reinjection on the left side of the beam. Assuming plane-wave propagation, the wave field at x_2 can be expressed as $V(x_2, \omega) = V(x_1, \omega)e^{ikd}$ in the Fourier domain, where k is the flexural wave number, $d = x_2 - x_1$ the propagation distance, and $V(x_1, \omega)$ is the wave field measured at x_1 . Thus, the experimental dispersion relation has to be determined.

The required dispersion relation is obtained by adopting the inhomogeneous wave correlation (IWC) method [33], which allows for calculation of the wave number by maximizing the correlation between a theoretical inhomogeneous running wave and the spatial response of the target over short measurement distances. We actuate the flexural A_0 Lamb mode on the right end of the beam and use the IWC method to determine the f - k relation of the host beam after the grading, i.e., for $x > 0.6$ m. Figure 7(a) shows the resulting dispersion relation, indicated by the black (dark) circles in the range of 0–1200 Hz. Assuming that the A_0 mode can be described by an exponential power-law function $k(\omega) = a\omega^b + c$, with $\omega = 2\pi f$, we use a least-squares solver to determine a continuous f - k relation in the frequency area of interest, indicated by the (light) blue line in Fig. 7(a). To verify the result, we forward propagate (reposition) the wave field measured at $x_1 = 0.7$ m [black line in Fig. 7(b)] by $d = 0.2$ m to $x_2 = 0.9$ m [red dashed line in Fig. 7(b)] and compare it to the measured wave field at x_2 [gray line in Fig. 7(b)], observing a good match.

Finally, the right-going wave field measured at 0.85 m with the IBC active [see Fig. 7(b)] is forward propagated from 0.85 to 1.0 m. To utilize the STF of the left actuator, where the wave field is reintroduced, the wave field is extrapolated an additional 0.1 m, such that its virtual recording position matches $x_{\text{LS}} = 0.1$ m, the measurement point for which $h_{\text{LS}}^{-1}(t)$ was determined. After applying the STF, the repositioned rightward-propagating wave is reintroduced into the beam on the left end. The newly arising reflections are again cancelled by iteratively constructing a secondary IBC on both ends of the beam. The schematic of the prototype geometry in Fig. 8(a) indicates that, as a result, the right end of the beam acts as a one-directional virtually periodic boundary. The time-distance plot in the same figure depicts the rightward-propagating wave field of the experimentally formed periodic boundary and Fig. 8(c) its normalized spatial-frequency representation.

A numerical COMSOL[®] [34] simulation is used to verify the observed experimental phenomena [see Figs. 8(b) and 8(d)]. The supercell of the numerical model, consisting of the 1-m-long host beam and the graded area, matches

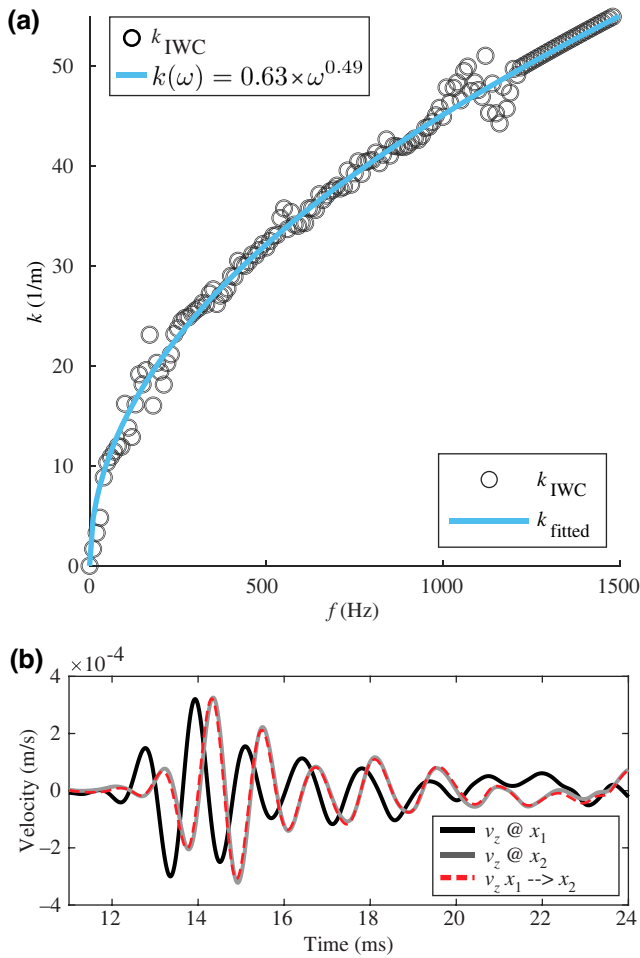


FIG. 7. (a) The dispersion relation as determined via the IWC method (black circles) and the fitted exponential function used for wave-field repositioning. (b) The forward redatuming of the measurement at $x_1 = 0.7$ m (black line) by 20 cm (dashed, red line) compared to the measurement at $x_2 = 0.9$ m (gray line).

the experimental prototype in its geometry. The material properties of the prototype are approximated by a Young's modulus of 69 GPa, a density of 2710 g/m³, and a Poisson ratio of 0.33. The supercell is replicated once, as indicated by the schematic in Fig. 8(b), to represent the periodic metamaterial. Comparing the experimental and numerical data, the band gap is deepened in both cases as the wave passes through the grading a second time. Furthermore, we find that the induced periodicity recovers the analytical solution of the periodic boundary condition (further details can be found in the Appendix). After the first pass through the supercell, the upper end of the band gap (dashed red line) converges to the analytical solution (solid red line) in both the experimental and the numerical results [Figs. 8(c) and 8(d)].

It is important to note that by reintroducing the wave field exiting on the right back at the left end, the back-scattered interactions between the virtually periodic graded

metamaterial are not accounted for in this experimental realization. These interactions are, however, included in the COMSOL simulation as the numerical model actually consists of two graded areas. This is where the differences in frequency content observable between 0.6 and 1.3 m in Figs. 8(c) and 8(d) might originate from. One additional difference observable is the missing energy content below 200 Hz in the virtually periodic experimental realization. Taking a closer look at the rightward-propagating wave fields in Figs. 8(a) and 8(b), we may note that the slower low-frequency portion of the propagating wave, which is clearly visible in the numerical simulation, is absent in the experimental realization during the second pass through the metamaterial [indicated by the red circle in Fig. 8(a)].

IV. DISCUSSION

The immersive boundary method that we implement paves a way toward further necessary exploration. First, the experimentally induced virtual periodicity in its current form accounts for the rightward-propagating waves, i.e., we can observe waves passing through sequential supercells of the grading and the resulting effect. However, the leftward-propagating waves, i.e., energy scattered at the graded resonator profile, are not accounted for. To include these interactions, construction of another virtual link is required. The second link would need to incorporate the leftward-propagating wave field reflected off the graded area after the first pass through. This wave field would then be reinjected at the right end of the structure. Second, by applying the IBCs far away from the graded area, we are introducing the periodicity based on the propagating wave field but not the evanescent nonpropagating component. However, the evanescent short-range interactions between the graded supercells could play an important role in the band-gap creation [35,36]. In the work flow presented, the direct wave must be properly separated from the reflections to determine the STF. Hence, at least one wavelength before the scattering is required. Moving the actuators and, thus, the IBC closer to the graded area is theoretically possible but would require a different approach to separate the wave fields. Finally, after the introduction of the virtual periodicity in Figs. 8(a) and 8(c), missing frequency content <200 Hz can be observed. When first applying the periodic signal, a new set of IBCs has to be constructed. To preserve the periodic signal in the process, it has to be separated from the new rightward-propagating unwanted reflections occurring at the left end through windowing. However, the much slower low-frequency component of the periodic signal is indistinguishable from these reflections. Consequently, the <200 Hz portion of the periodic signal is erroneously included in the first iteration of the new IBC and removed through its application. Instead of utilizing visual windowing, the two wave-field components could be separated by subtracting the predicted

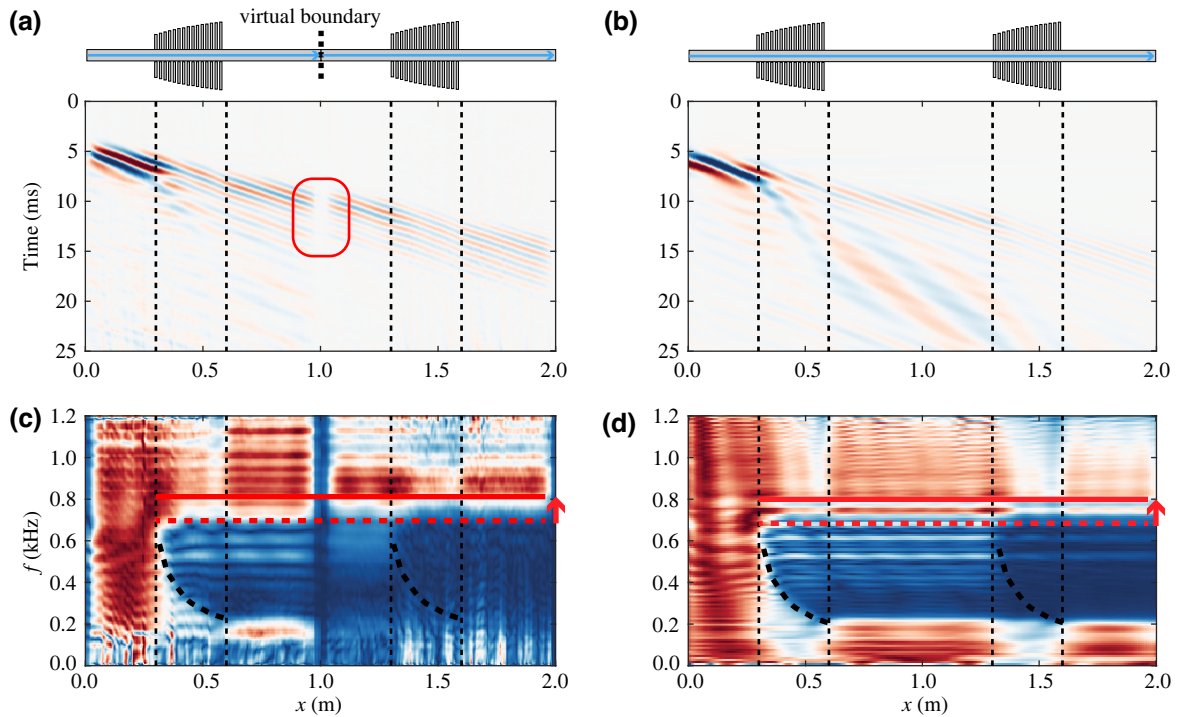


FIG. 8. A time-distance representation of the right-going out-of-plane velocity measured along the beam. (a) The experimental data: the red box indicates where the rightward-propagating wave field is reintroduced on the left end, making it appear as though the wave is propagating through a continuous medium with two sequential graded areas. (b) The numerical simulation of two sequential graded supercells and the resulting rightward wave-field propagation. (c),(d) The respective normalized spatial-frequency representation of (a) and (b). The dashed red line indicates the upper end of the band gap after a single pass through the supercell. After the second pass through, a widening of the band gap and convergence to the analytical solution (solid red line) are observable in both the experimental and the numerical results.

periodic signal from the full rightward-propagating wave field.

The examples presented in this work showcase propagating waves of a singular mode, with limited spatial and temporal width, i.e., traveling-wave packages. In this first realization, such propagation is desirable, as it makes identification of the direct wave and its first- to higher-order reflections feasible. However, our proposed work flow could also be applied to periodic signals, such as continuous sinusoidal excitation of the metamaterial. In fact, the signature of the propagating wave field confined to the first 30 cm of the metamaterial, i.e., before the grading, which is observable in Fig. 7(a), has strong similarities to standing waves emerging during periodic excitation. Indeed, the signature of the designed IBC on the left end of the beam, as depicted in Fig. 7(b), resembles a continuous sinusoidal excitation. Hence, by manipulating the boundary conditions, our methodology could be used to, e.g., transform standing waves to traveling waves and enrich the data sampled along the metamaterial under investigation. The possible advantages of such an experimental tool have recently been discussed for an acoustic impedance tube [37].

It is well known that metamaterials also support propagation modes other than the flexural A_0 mode utilized in this study, such as dilatation and torsional modes [38–40]. As mentioned, in this first demonstration of elastic IWE, an effort is made to prevent mode conversions from occurring at the ends of the beam. Nevertheless, elastic IWE is also suitable for simultaneously operating on different propagation modes and polarities [20]. When utilizing the reflected wave field, as presented here, the IBCs would need to be constructed for each of the three propagation components. Thus, multicomponent actuators are key for an effective realization. Note that if the first-order incident traction can be defined, rather than the reflected wave field, its application directly cancels all mode conversions occurring at the domain ends, as per the IWE theory presented by Thomsen *et al.* [20]. Control of which modes are cancelled by the IBC further allows us to study how different types of boundary conditions influence the band structures observed in the metamaterial under study [41].

Due to the possibilities offered by boundless metamaterial experimentation, a real-time implementation of the method presented here is highly desirable. However, a real-time realization of elastic IWE is challenging and

its feasibility strongly depends on the experimental conditions. Whereas acoustic implementations of IWE have been achieved in real time [42], the much larger wave speeds in solids, when compared to air or fluids, are the strongest limiting factor. Enough time is needed to predict the wave field incident on the boundary where the desired manipulation via IWE is to take place. If the location where the wave field is recorded and the IBC applied are the same, a real-time implementation is not possible. Nevertheless, in a setup similar to the one presented here, where recordings can be made along the wave-propagation path, a real-time implementation could be possible with sufficiently fast hardware. In any case, it is necessary to extrapolate the wave field from the recording to the emitting boundary and, thus, a prior characterization of a homogeneous portion of the medium under investigation is required. The feasibility could be further increased by utilizing manufactured materials with much lower wave speeds, such as foams or plastics.

We would like to point out that our proposed methodology has similarities to “surface related multiple removal” [43], commonly applied in the field of geophysics. However, our method does not rely on the prediction of the multiple reflections occurring at the domain boundaries but, rather, is fully data driven, assuming only linear wave propagation.

Finally, full three-dimensional (3D) three-component elastic IWE, as proposed by Vasmel [21] and Thomsen *et al.* [20], has yet to be realized experimentally. To this end, Thomsen *et al.* [25] have proposed a numerical wave-field injection-based methodology to retrieve the primary incident wave field when only recordings of the three-component particle velocity at the free surface are available. However, the method requires a full characterization of the physical experimental domain. Recently, Li *et al.* [44] have bypassed this—in most experimental cases, unfeasible—requirement by incorporating an internal absorbing boundary in the wave-field injection scheme, resulting in the retrieval of the *full* incident and reflected wave fields. Consequently, this wave-field injection scheme could be combined with our proposed iterative work flow to utilize the *full* reflected wave field in designing the IBC instead of only the primary incident wave field.

V. CONCLUSIONS

We introduce an approach to the experimental investigation and validation of metamaterial prototypes that provides a fully data-driven work flow to implement active boundary control in the presence of strongly dispersive wave propagation and internal scattering. Through the design of IBCs, reflection suppression, virtual periodicity, and the introduction of fictitious boundaries are enabled. The IBC is constructed iteratively by injection of the

polarity-reversed full wave field reflected at the target boundaries. Higher-order reflections are removed step by step by adapting the IBC during each experimental iteration. Our *ad hoc* work flow circumvents the requirement of a perfect free-surface boundary to act on with the IBC, as defined by elastic IWE theory [20,23], working purely with the reflected wave field, and requires no knowledge of the medium under investigation. Thus, it permits any experimental conditions, such as clamped boundaries or those deviating from perfect free surfaces due to the influence of attached actuators. In a first experimental proof of concept, a one-directional virtual periodic boundary condition is created in an elastic metamaterial by reintroducing waves leaving the structure on one end back into the opposite end. As a result, the experimental band gap observed converges to the analytical solution. This experimental realization of a “Bloch-like” geometric periodicity has the potential to facilitate the study of metamaterials without the need to physically realize large structures in the laboratory. Instead, only one to a few unit cells are required. Boundless experimentation can thus act as a powerful tool in future metamaterial research.

ACKNOWLEDGMENTS

This research was supported by the European Union Horizon 2020 Future and Emerging Technologies (FET)-proactive Metamaterial Enhanced Vibration Energy Harvesting (METAVEH) project under Grant Agreement No. 952039, the European Research Council (ERC) Grant No. 694407—Machine for Time Reversal and Immersive Wave Experimentation (MATRIX), and the Swiss National Science Foundation (SNSF) Research Equipment (R’Equip) Grant No. 206021_205418.

APPENDIX: CONVERGENCE TO ANALYTICAL BANDGAP

As is observable in Fig. 8(c), the experimental band gap widens when the virtual periodicity is introduced. This phenomenon can be understood as the experimental realization converging to the analytical solution.

Recently, Pu *et al.* [45] have proposed a multiscatter formulation to analytically describe the out-of-plane component $w(x)$ of a wave at position x propagating along a host beam and interacting with N resonators as

$$w(x) = w_0(x) + \sum_{n=1}^N Q_n G_w(x - x_n). \quad (\text{A1})$$

Here, $w_0(x)$ represents the wave field at position x incident at the base of N parasitic wing pairs. The term Q_n describes the amplitude of the uniform normal stress at the base of the n th pair of wings attached to the host beam. G_w is the related out-of-plane displacement Green’s function [46].

Together these terms compute the scattered wave field of the N parasitic wing pairs. The normal stress amplitude Q_n can be found from the mechanical impedance via

$$Q_n = \frac{2M_n\omega_{rn}^2\omega^2}{S_n(\omega_{rn}^2 - \omega^2)}w(x_n) = Z_n w(x_n), \quad (\text{A2})$$

where $\omega_{rn} = \sqrt{K_n/M_n}$ is the resonant frequency of the n th pair of parasitic wings. Together with the mechanical impedance Z_n , the amplitude Q_n can be computed knowing

$$\mathbf{A}\mathbf{X} = \mathbf{0}, \quad (\text{A3})$$

with

$$\mathbf{A} = \begin{bmatrix} Z_1^{-1} - G_w(0) & -G_w(x_1 - x_2) & \cdots & -G_w(x_1 - x_N) \\ -G_w(x_2 - x_1) & Z_2^{-1} - G_w(0) & \cdots & -G_w(x_2 - x_N) \\ \vdots & \vdots & \ddots & \vdots \\ -G_w(x_N - x_1) & -G_w(x_N - x_2) & \cdots & Z_N^{-1} - G_w(0) \end{bmatrix}, \quad \mathbf{X} = \begin{bmatrix} Q_1 \\ Q_2 \\ \vdots \\ Q_N \end{bmatrix}. \quad (\text{A4})$$

The virtual periodicity introduced via our proposed method only accounts for rightward-propagating waves and neglects the interactions between supercells. A supercell describes one element of the host beam plus graded parasitic wings as illustrated in Fig. 8(a). Consequently, this extended eigenvalue problem can be formulated as

$$\mathbf{A}_E\mathbf{X}_E = \mathbf{0}, \quad (\text{A5})$$

with

$$\mathbf{A}_E = \begin{bmatrix} \mathbf{A}_1 & & & \\ & \mathbf{A}_2 & & \\ & & \ddots & \\ & & & \mathbf{A}_N \end{bmatrix}, \quad \mathbf{X}_E = \begin{bmatrix} \mathbf{X}_1 \\ \mathbf{X}_2 \\ \vdots \\ \mathbf{X}_N \end{bmatrix}, \quad (\text{A6})$$

where \mathbf{A}_1 to \mathbf{A}_N describe the periodically arranged supercells. Comparing Eqs. (A6) to (A4), this configuration has the same eigenvalues corresponding to the band-gap ranges of a singular supercell of the metamaterial. Thus, by introducing the virtual geometric periodicity experimentally, we converge to the analytical solution of the eigenvalue problem determining the metamaterials band gap.

the vertical displacement $w(x_n)$ at the base of the n th parasitic wing pair. Thus, given an incident wave field $w_0(x)$, the stress amplitudes can be computed and the total wave field obtained using Eq. (A1).

Assuming a null incident field with $w_0 = 0$, the eigenstates of the system can be obtained in matrix form via Eqs. (A1) and (A2) from the eigenvalue problem

[1] K. Bertoldi, P. M. Reis, S. Willshaw, and T. Mullin, Negative Poisson's ratio behavior induced by an elastic instability, *Adv. Mater.* **22**, 361 (2010).

[2] X. Zheng, H. Lee, T. H. Weisgraber, M. Shusteff, J. DeOtte, E. B. Duoss, J. D. Kuntz, M. M. Biener, Q. Ge, and

J. A. Jackson, *et al.*, Ultralight, ultrastiff mechanical metamaterials, *Science* **344**, 1373 (2014).

[3] Y. Wang, L. Li, D. Hofmann, J. E. Andrade, and C. Daraio, Structured fabrics with tunable mechanical properties, *Nature* **596**, 238 (2021).

[4] A. Colombi, D. Colquitt, P. Roux, S. Guenneau, and R. V. Craster, A seismic metamaterial: The resonant metawedge, *Sci. Rep.* **6**, 1 (2016).

[5] K. H. Matlack, A. Bauhofer, S. Krödel, A. Palermo, and C. Daraio, Composite 3D-printed metastructures for low-frequency and broadband vibration absorption, *Proc. Natl. Acad. Sci.* **113**, 8386 (2016).

[6] M. M. Sigalas and E. N. Economou, Elastic and acoustic wave band structure, *J. Sound. Vib.* **158**, 377 (1992).

[7] Z. Liu, X. Zhang, Y. Mao, Y. Zhu, Z. Yang, C. T. Chan, and P. Sheng, Locally resonant sonic materials, *Science* **289**, 1734 (2000).

[8] R. V. Craster and S. Guenneau, *Acoustic Metamaterials: Negative Refraction, Imaging, Lensing and Cloaking* (Springer Science & Business Media, Dordrecht, Netherlands, 2012), Vol. 166.

[9] J. M. De Ponti, A. Colombi, E. Riva, R. Ardito, F. Braghin, A. Corigliano, and R. V. Craster, Experimental investigation of amplification, via a mechanical delay-line, in a rainbow-based metamaterial for energy harvesting, *Appl. Phys. Lett.* **117**, 143902 (2020).

[10] J. M. De Ponti, A. Colombi, R. Ardito, F. Braghin, A. Corigliano, and R. V. Craster, Graded elastic metasurface for enhanced energy harvesting, *New J. Phys.* **22**, 013013 (2020).

[11] J. M. De Ponti, L. Iorio, E. Riva, F. Braghin, A. Corigliano, and R. Ardito, Enhanced energy harvesting of flexural waves in elastic beams by bending mode of graded resonators, *Front. Mater.* **8**, 745141 (2021).

[12] B. Zhao, H. R. Thomsen, J. M. De Ponti, E. Riva, B. Van Damme, A. Bergamini, E. Chatzi, and A. Colombi,

- A graded metamaterial for broadband and high-capability piezoelectric energy harvesting, *Energy Convers. Manage.* **269**, 116056 (2022).
- [13] D. Komatitsch and R. Martin, An unsplit convolutional perfectly matched layer improved at grazing incidence for the seismic wave equation, *Geophysics* **72**, SM155 (2007).
- [14] P. Rajagopal, M. Drozd, E. A. Skelton, M. J. Lowe, and R. V. Craster, On the use of absorbing layers to simulate the propagation of elastic waves in unbounded isotropic media using commercially available finite element packages, *NDT E. Int.* **51**, 30 (2012).
- [15] M. Mironov, Propagation of a flexural wave in a plate whose thickness decreases smoothly to zero in a finite interval. *Sov. Phys. Acoust.—USSR* **34**, 318 (1988).
- [16] D. O'Boy, V. Krylov, and V. Kralovic, Damping of flexural vibrations in rectangular plates using the acoustic black hole effect, *J. Sound Vib.* **329**, 4672 (2010).
- [17] V. Georgiev, J. Cuenca, F. Gautier, L. Simon, and V. Krylov, Damping of structural vibrations in beams and elliptical plates using the acoustic black hole effect, *J. Sound Vib.* **330**, 2497 (2011).
- [18] A. Pelat, F. Gautier, S. C. Conlon, and F. Semperlotti, The acoustic black hole: A review of theory and applications, *J. Sound Vib.* **476**, 115316 (2020).
- [19] C. Vemula, A. Norris, and G. Cody, Attenuation of waves in plates and bars using a graded impedance interface at edges, *J. Sound Vib.* **196**, 107 (1996).
- [20] H. R. Thomsen, M. Molerón, T. Haag, D.-J. van Manen, and J. O. A. Robertsson, Elastic immersive wave experimentation: Theory and physical implementation, *Phys. Rev. Res.* **1**, 033203 (2019).
- [21] M. Vasmel, Doctoral Thesis, Department of Earth Sciences, ETH Zürich, Zürich, Switzerland, 2016.
- [22] N. Börsing, T. S. Becker, A. Curtis, D.-J. van Manen, T. Haag, and J. O. Robertsson, Cloaking and Holography Experiments Using Immersive Boundary Conditions, *Phys. Rev. Appl.* **12**, 024011 (2019).
- [23] T. S. Becker, N. Börsing, T. Haag, C. Bärlocher, C. M. Donahue, A. Curtis, J. O. A. Robertsson, and D.-J. van Manen, Real-Time Immersion of Physical Experiments in Virtual Wave-Physics Domains, *Phys. Rev. Appl.* **13**, 064061 (2020).
- [24] D.-J. van Manen, M. Moleron, H. R. Thomsen, N. Börsing, T. S. Becker, M. R. Haberman, and J. O. Robertsson, Immersive boundary conditions for meta-material experimentation, *J. Acoust. Soc. Am.* **146**, 2786 (2019).
- [25] H. R. Thomsen, E. F. M. Koene, J. O. A. Robertsson, and D.-J. van Manen, FD-injection-based elastic wavefield separation for open and closed configurations, *Geophys. J. Int.* **227**, 1646 (2021).
- [26] L. Sønneland, L. E. Berg, P. Eidsvig, A. Haugen, B. Fotland, and J. Vestby, in *SEG Technical Program Expanded Abstracts 1986, Vol. 4* (Society of Exploration Geophysicists, 1986), p. 516.
- [27] B. A. Hardage, Vertical seismic profiling, *Leading Edge* **4**, 59 (1985).
- [28] PI Ceramic GmbH, PICA Shear Actuators, (2018).
- [29] Polytec GmbH, PSV-500-3D Scanning Vibrometer, (2019).
- [30] See the Supplemental Material at <http://link.aps.org/supplemental/10.1103/PhysRevApplied.19.064019> for animations of the out-of-plane velocity component as measured by a LDV along the metamaterial.
- [31] K. Tsakmakidis, A. Boardman, and O. Hess, Nature: Trapped rainbow storage of light in metamaterials, *Nature* **450**, 397 (2007).
- [32] J. M. De Ponti, L. Iorio, E. Riva, R. Ardito, F. Braghin, and A. Corigliano, Selective Mode Conversion and Rainbow Trapping via Graded Elastic Waveguides, *Phys. Rev. Appl.* **16**, 034028 (2021).
- [33] B. Van Damme and A. Zemp, Measuring dispersion curves for bending waves in beams: A comparison of spatial Fourier transform and inhomogeneous wave correlation, *Acta. Acust. United Acust.* **104**, 228 (2018).
- [34] COMSOL AB, COMSOL Multiphysics v. 5.6, (2022).
- [35] F. Lemoult, G. Lerosey, J. de Rosny, and M. Fink, Resonant Metalenses for Breaking the Diffraction Barrier, *Phys. Rev. Lett.* **104**, 203901 (2010).
- [36] F. Lemoult, M. Fink, and G. Lerosey, Acoustic Resonators for Far-Field Control of Sound on a Subwavelength Scale, *Phys. Rev. Lett.* **107**, 064301 (2011).
- [37] Y. Vered and I. Bucher, Experimental multimode traveling waves identification in an acoustic waveguide, *Mech. Syst. Signal Process.* **153**, 107515 (2021).
- [38] S. Jiang, H. Hu, and V. Laude, Low-frequency band gap in cross-like holey phononic crystal strip, *J. Phys. D: Appl. Phys.* **51**, 045601 (2018).
- [39] E. Coffy, T. Lavergne, M. Addouche, S. Euphrasie, P. Vairac, and A. Khelif, Ultra-wide acoustic band gaps in pillar-based phononic crystal strips, *J. Appl. Phys.* **118**, 214902 (2015).
- [40] E. Coffy, S. Euphrasie, M. Addouche, P. Vairac, and A. Khelif, Evidence of a broadband gap in a phononic crystal strip, *Ultrasonics* **78**, 51 (2017).
- [41] F.-C. Hsu, C.-I. Lee, J.-C. Hsu, T.-C. Huang, C.-H. Wang, and P. Chang, Acoustic band gaps in phononic crystal strip waveguides, *Appl. Phys. Lett.* **96**, 051902 (2010).
- [42] T. S. Becker, D.-J. van Manen, T. Haag, C. Bärlocher, X. Li, N. Börsing, A. Curtis, M. Serra-Garcia, and J. O. A. Robertsson, Broadband acoustic invisibility and illusions, *Sci. Adv.* **7**, eabi9627 (2021).
- [43] R. Abma, N. Kabir, K. H. Matson, S. Michell, S. A. Shaw, and B. McLain, Comparisons of adaptive subtraction methods for multiple attenuation, *Leading Edge* **24**, 277 (2005).
- [44] X. Li, J. Robertsson, A. Curtis, and D.-J. van Manen, Internal absorbing boundary conditions for closed-aperture wavefield decomposition in solid media with unknown interiors, *J. Acoust. Soc. Am.* **152**, 313 (2022).
- [45] X. Pu, A. Palermo, and A. Marzani, Topological edge states of quasiperiodic elastic metasurfaces, *Mech. Syst. Signal Process.* **181**, 109478 (2022).
- [46] K. F. Graff, *Wave Motion in Elastic Solids* (Courier Corporation, 2012).